ENGINEERING

Water vapor capturing using an array of traveling liquid beads for desalination and water treatment

A. Sadeghpour[1]*, Z. Zeng[1]*, H. Ji[2], N. Dehdari Ebrahimi[1], A. L. Bertozzi[1,2], Y. S. Ju[1†]

Growing concern over the scarcity of freshwater motivates the development of compact and economic vapor capture methods for distributed thermal desalination or harvesting of water. We report a study of water vapor condensation on cold liquid beads traveling down a massive array of vertical cotton threads that act as pseudo-superhydrophilic surfaces. These liquid beads form through intrinsic flow instability and offer localized high-curvature surfaces that enhance vapor diffusion toward the liquid surface, a critical rate-limiting step. As the liquid flow rate increases, the bead spacing decreases, whereas the bead size and speed stay nearly constant. The resulting increase in the spatial bead density leads to mass transfer conductances and hence condensation rates per volume that are almost three times higher than the best reported values. Parallel and contiguous gas flow paths also result in a substantial reduction in gas pressure drop and hence electric fan power consumption.

INTRODUCTION

Freshwater is a precious and scarce resource. Recent studies projected that severe droughts and other extreme weather events will occur at ever more increasing intensities and frequencies, placing greater strains on already limited freshwater resources in many parts of the world. Researchers found that more than half of the global population lives in areas with severe water scarcity condition for more than 1 month per year (*1*). Previous and ongoing research efforts have led to the development and refinement of various solutions for this problem such as desalination and water treatment technologies, including reverse/forward osmosis, nanofiltration, electrodialysis, and thermal distillation. Other novel approaches, such as ambient moisture harvesting (*2*, *3*) and fog/mist collection (*4*), have also received increasing attention.

Water vapor capture is an integral part of many freshwater production methods, including aforementioned ambient moisture harvesting, vapor recovery from cooling towers in thermoelectric power plants, and ambient-pressure humidification-dehumidification (HDH) desalination systems. The HDH desalination system is an intriguing desalination and water treatment approach (*5*), which imitates the natural rain cycle by creating humidified air (e.g., blowing dry air over a heated brine) and then condensing water vapor, using a water vapor–capturing device (hereinafter referred to as "dehumidifier"), to produce distilled water. It is attractive for small-scale distributed desalination and water treatment because they are very tolerant to high salinity and can produce high-quality (distilled) water using a wide variety of feed water streams, including industrial and agricultural wastewater, produced water from oil/gas fields, contaminated ground water, and brine discharge from reverse osmosis or membrane filtration plants.

The critical technical challenge of HDH lies in improving thermal energy efficiency. Previous studies (*6*–*9*) proposed approaches to thermodynamically balancing humidification and dehumidification processes and reported designs with energy efficiency competitive with other technologies while delivering benefits of reduced capital and operation costs.

A practical limit in thermal efficiency, however, is posed by heat/mass exchange processes. Particularly problematic is dehumidification, which suffers from inherently large resistance to mass transfer experienced by water vapor as it diffuses through air. The deleterious effects of noncondensable gases on condensation have been well documented (*10*, *11*). Noncondensable gases of a volume fraction as low as 0.5% have been observed to cause as much as 50% reduction in condensation heat transfer.

Conventional approaches to condensation rely on cooled solid surfaces in contact with a gas stream, which is a mixture of the target vapor and other noncondensable gases. One can theoretically achieve high mass transfer rates by using densely packed solid surfaces of large surface areas to reduce average distances that vapor molecules must diffuse through. However, because of constraints on weight, cost, and/or manufacturability, solid surface areas per volume that one can achieve are limited. Other methods, such as enhanced convective mixing through intermittent liquid feeds (*12*) and electric winds generated by corona discharge (*13*), can enhance mass transfer but at the expense of increased power consumption and complexity. More recent studies adapted bubble columns for dehumidification (*14*), where humidified air is injected through a pool of cooled water to create bubbles with large surface-to-volume ratios for enhanced heat and mass transfer. The very large pressure head required to sustain air flows, however, again leads to increased electricity consumption.

Here, we report our experimental study of interfacial flow and phase change phenomena in a unique configuration where water vapor in a humidified air stream is condensed on traveling water beads. The traveling water beads themselves are generated by the intrinsic instability of thin liquid films flowing down an array of vertical threads (Fig. 1) without requiring the use of spray nozzles or application of electric fields.

The unique geometric configuration presents an intriguing model system for heat and mass transfer by offering (i) very high interface-to-volume ratios in a compact volume, (ii) efficient mass diffusion of vapor toward local curved surface features (liquid beads) that act as sinks, and (iii) long residence times of liquid beads for mass transfer. The long residence time is enabled by viscous shear stress exerted by the cotton thread surface, which opposes downward sliding motion of liquid beads.

Despite offering high interface-to-volume ratios, the multistring array introduces small pressure drops for gas flows in part because it provides straight, open and contiguous gas flow paths and in part because low-profile traveling liquid beads present relatively small form drag (*15*–*18*).

[1]Mechanical and Aerospace Engineering Department, University of California–Los Angeles, Los Angeles, CA 90095, USA. [2]Department of Mathematics, University of California–Los Angeles, Los Angeles, CA 90095, USA.
*These authors contributed equally to this work.
†Corresponding author. Email: sungtaek.ju@ucla.edu

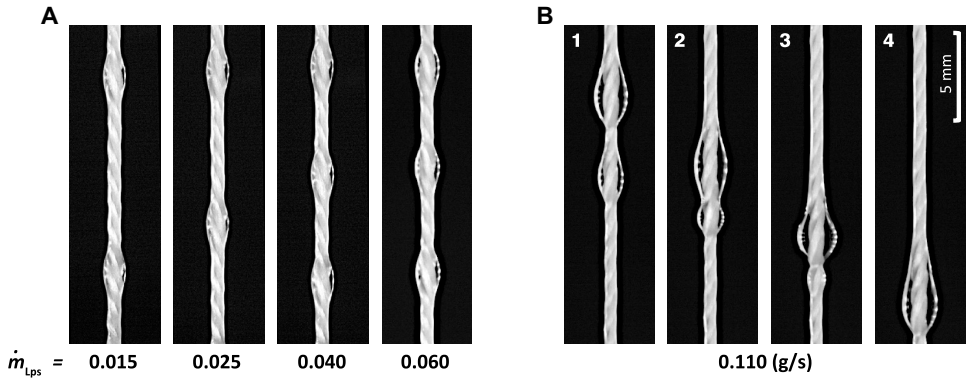

Fig. 1. Water flow regimes. Water flowing down a cotton thread with a diameter of 0.76 mm at flow rates of (**A**) $\dot{m}_{Lps}$ = 0.015 to 0.06 g/s, resulting in the Rayleigh-Plateau instability regime, where beads have constant velocities and spacings, and (**B**) $\dot{m}_{Lps}$ = 0.11 g/s, generating a flow in the convective instability regime that features bead coalescence (Nozzle inner diameter = 0.8 mm).

In our recent paper (*19*), we reported an early demonstration of thin film flows of water along cotton threads and their potential application in evaporation/humidification. This early demonstration, however, was rather ad hoc and incomplete, as we merely relied on trial and error to select thread diameters and liquid flow rates without proper theoretical understanding of fluid mechanics or heat and mass transfer processes involved. Furthermore, although experimental data on the evaporation rates were obtained, they were limited and we could only discuss qualitative trends over narrow ranges of flow parameters. Last, the improvement in the performance over the existing state-of-the-art humidifier was appreciable but not dramatic.

The present paper substantially builds upon this early work and reports a dehumidifier that offers 200% improvement in the condensation rate per volume than the current states of the art, which are heavy and expensive or involves very large pressure drops. To establish firm scientific foundation, we performed the first-ever combined experimental and theoretical study of the instability in thin film flows of a high–surface energy low-viscosity liquid. This allows us to develop a theoretical framework to identify threshold flow rates for transition between two different instability regimes. We also report a complementary numerical model that solves the full Navier-Stokes equations to quantitatively capture the details of flow patterns while accounting for the impact of surface roughness inherent in cotton threads. In addition, our systematic experiments of heat and mass transfer provide data to develop and validate an analytic model for dehumidification and to quantify the impact of transition between the flow instability regimes on heat and mass transfer processes.

RESULTS

Instability in thin water films flowing down vertical strings

Because of the interplay among surface tension, viscous, inertial, and gravitational forces, liquid films flowing down vertical strings develop complex flow patterns (*20*–*24*). The insets in Fig. 1 show still images of wavy liquid films, representing discrete traveling liquid beads formed by intrinsic flow instability. We shall show that these wavy patterns help substantially enhance mass transfer and thereby condensation of water vapor.

As shown in Fig. 1A, thin liquid films flowing down a string may exhibit absolute instability where the surface tension and viscous forces primarily govern flow dynamics, with liquid beads of a fixed size traveling at a constant speed and interval (i.e., a fixed wavelength of wavy patterns). This is often referred to as the Rayleigh-Plateau regime. When inertia becomes important, thin film flows may exhibit convective instability where liquid beads travel at different speeds, merging and subsequently forming new beads. Figure 1B illustrates coalescence of water beads in the convective instability regime. These different instability modes can be captured in spatiotemporal diagrams, which schematically represent the temporally evolving positions of liquid beads along the string (fig. S1).

Previous experimental studies of the flow instability in question almost exclusively used well-wetting low–surface energy liquids of high viscosities, such as silicone oil. Water is a high–surface energy low-viscosity liquid, where the influence of surface tension is much more pronounced. As water does not wet common polymeric strings, previous studies used a carefully cleaned glass wire to achieve a thin film flow in the absolute instability regime (*17*); however, such a fragile material is not practical for engineering applications. Here, we use cotton threads that absorb water into their porous structures and essentially function as superhydrophilic strings.

Mathematical modeling of water film flows on cotton thread

Earlier studies of thin liquid films flow along strings used low surface tension fluids of relatively high viscosities, whose main flow characteristics can be captured using one-dimensional lubrication and related models. Our thin water film flows have much higher characteristic Reynolds numbers, and the effects of inertia and nozzles cannot be ignored. We numerically solve the Naiver-Stoke equations to predict the characteristics of water flowing down a vertical cotton thread such as bead size and bead spacing. We observe that incorporating an effective boundary slip induced by the surface roughness on cotton threads is essential in correctly capturing the flow pattern because of the fact that the smooth surface assumption leads to an underestimation of the bead frequency by more than 30%. As shown in Fig. 2A, we define the slip coefficient, λ, as the average amplitude of the surface roughness of cotton thread (*25*), which was found to be ~0.04 mm for our cotton threads based on the image analysis study. Further details of the numerical simulation are provided in section S1. Figure 2B shows that a flow pattern predicted in our numerical stimulation is consistent with the experimental result for a string diameter D_s = 0.76 mm, a nozzle inner diameter of 1.2 mm, an average surface roughness λ = 0.04 mm at the string surface, and a water flow rate $\dot{m}_{Lps}$ = 0.12 g/s. Figure 2C

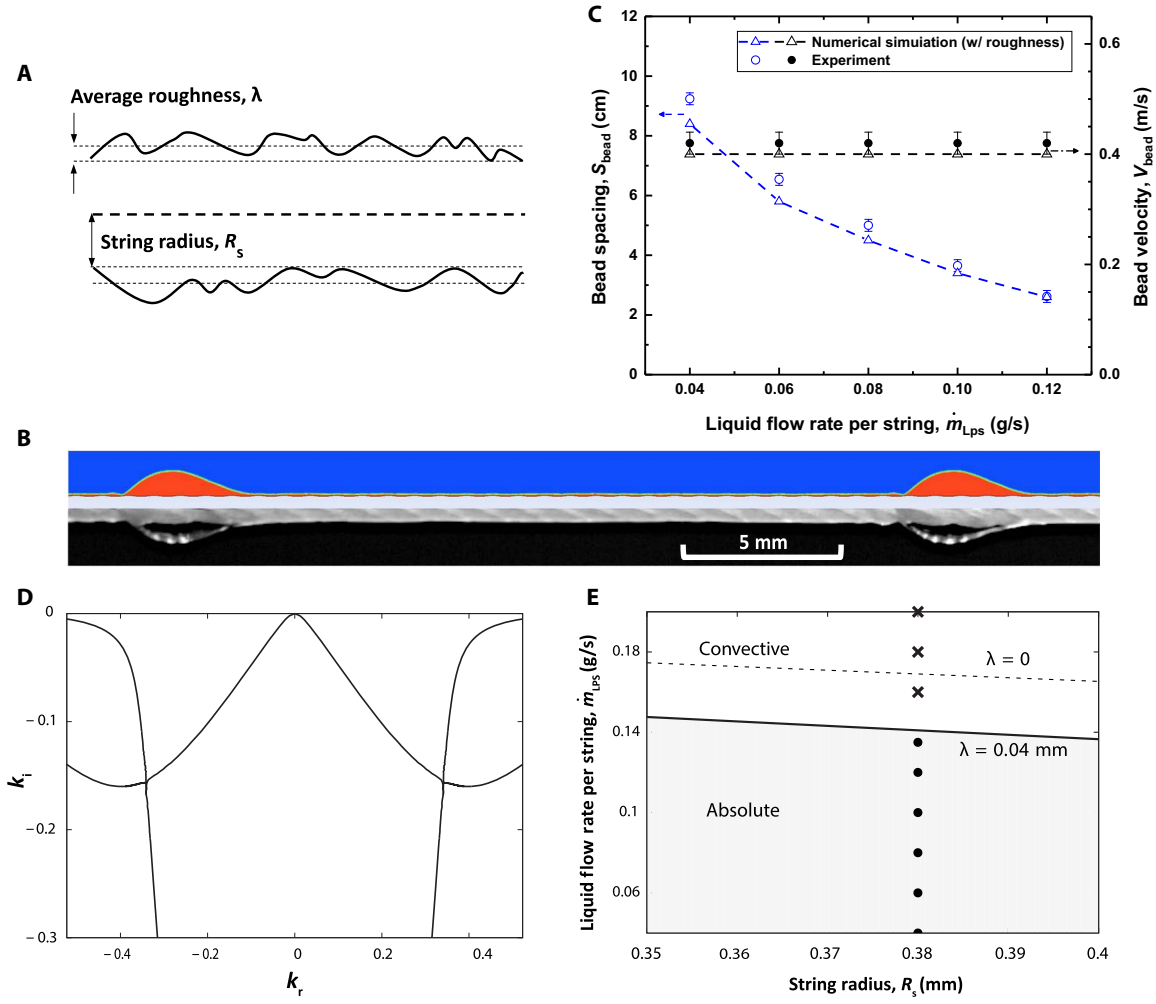

Fig. 2. Mathematical and numerical modeling. (**A**) Schematic of a cotton thread with radius R_s and average roughness λ. (**B**) Comparison of the experimentally obtained liquid profile and the results obtained from the full Navier-Stokes numerical simulation (string diameter D_s = 0.76 mm, the nozzle inner diameter = 1.2 mm, liquid mass flow rate $\dot{m}_{Lps}$ = 0.12 g/s, and average roughness λ = 0.04 mm). (**C**) The bead spacing and velocity predicted from full Navier-Stokes numerical simulation compared with experimental results (D_s = 0.76 mm, nozzle inner diameter = 1.2 mm, $\dot{m}_{Lps}$ = 0.04 to 0.12 g/s, and λ = 0.04 mm). (**D**) Spatial branches in the complex *k*-plane from the Orr-Sommerfeld (OS) analysis for a liquid flow rate of 0.141 g/s, string diameter of 0.76 mm, effective slip length of 0.04 mm, and $\omega_i = 0$. (**E**) The absolute and convective instability regimes in the parameter plane of the flow rate versus the string radius. The solid line corresponds to the OS solutions with roughness-induced boundary slip, and the dashed line corresponds to the no-slip case. The circle and cross symbols represent the regularly and irregularly spaced liquid beads observed in the experiments, respectively.

shows that the experimental results, which are measured by image analysis, and numerical simulation results for bead spacing, S_{bead}, and bead velocity, V_{bead} agree to within 10%.

As we shall discuss further in the subsequent section, with increasing liquid flow rates, the mass transfer rate of water vapor is generally enhanced. When the film flow transitions from the absolute to the convective instability regime, however, the emergence of irregular bead patterns in the convective regime suppresses further growth in the mass transfer rate with continued increase in the liquid mass flow rate. Identifying the critical flow rate for the instability regime transition is therefore important.

We apply the Orr-Sommerfeld (OS) analysis to investigate the transition. The OS equation derived from linearization of the Navier-Stokes equation is a fourth-order differential equation for the complex perturbation stream function amplitude $\Psi(r)$. The form of the perturbation is given by $\psi(r, t) = \Psi(r)\exp(i(kx - \omega t))$, where $k = k_r + ik_i$ and $\omega = \omega_r + i\omega_i$. In the complex (k_r, k_i) plane, two disconnected spatial branches merge together at a point that corresponds to the zero group velocity, $v_g = d\omega/dk = 0$. This defines the absolute wave number k_0 and the absolute frequency ω_0. A zero group velocity with $\omega_{0i} > 0$ identifies the onset of the absolute instability, and the instability regime transition occurs when the two branches merge at a point that corresponds to a real absolute frequency. Figure 2D shows an example of the merging of branches of the OS solutions at a critical flow rate.

Previous OS studies (*21*, *26*) for cylindrical falling films assumed smooth surfaces and applied the no-slip boundary condition at the liquid-solid interface. However, we find that this assumption leads to an overestimation of the critical flow rate by nearly 20% (Fig. 2E). As mentioned before, we approximately account for the finite roughness of cotton thread surfaces by introducing the Navier slip condition at the string surface ($r = R_s$)

$$\frac{d\psi}{dr} + \lambda \frac{d^2\psi}{dr^2} = 0 \quad (1)$$

where R_s is the average string radius. This approximation represents homogenization of the no-slip condition on rough surfaces and is sometimes referred to as the Navier friction condition. To account for uncertainty in measured values of the string radius, we perform the OS analysis for a range of string radius values, 0.35 mm $\leq R_s \leq$ 0.4 mm, and compare the predicted critical flow rates for $\lambda = 0$ (no slip) and $\lambda = 0.04$ mm in Fig. 2E. Our results show that the surface roughness $\lambda = 0.04$ mm produces decreased unperturbed flow velocities and yields a smaller critical flow rate, which is consistent with our experimental observations.

Condensation rates: Mass transfer conductance

Direct determination of the condensation rate from the difference between the inlet and outlet liquid flow rates is challenging because of fluctuations in the inlet and outlet flow rates and uncontrolled evaporation in and around the inlet and outlet reservoirs. We instead analyze axial temperature profiles (fig. S3) using the energy and mass balance equations to indirectly calculate the rate of mass transfer of water vapor from the humidified air stream to the liquid films flowing down the threads. The mass transfer conductance, g_m, which has the unit of mass flux [in kg/(m^{2}s)], is a proportionality factor for mass transfer rates. It is defined as $\rho_m D_{12}/\delta$, where ρ_m is the density of the air/water mixture, D_{12} is the binary diffusion coefficient of water vapor in air, and δ is the thickness of mass transfer boundary layer.

The balance equations are derived by applying the mass and energy conservation principle to a differential control volume shown in Fig. 3A. The mass balance equations for the water and air streams are

$$\dot{m}_{w,2} - \dot{m}_{w,1} = g_m[m_1(T_{a,1}) - m_1(T_{w,1})]dA \quad (2)$$

$$\dot{m}_{a,2} - \dot{m}_{a,1} = \dot{m}_{w,2} - \dot{m}_{w,1} \quad (3)$$

Here, $\dot{m}$ is the mass flow rate and the subscripts a and w denote the properties of the saturated air and water, respectively. $m_1(T_{a,1})$ and $m_1(T_{w,1})$ are the mass fractions of water in the saturated air at temperatures $T_{a,1}$ and $T_{w,1}$, respectively. We define dA as the nominal air-water interfacial area in the control volume. For mathematical convenience, we assume a perfect cylinder of water flowing down the cotton thread. The radius of the water cylinder was obtained from the Nusselt solution based on the experimentally measured water mass flow rates (*23*). The energy balance equation for the combined air and water stream in terms of their enthalpy h is

$$\dot{m}_{a,2}h_{a,2} - \dot{m}_{a,1}h_{a,1} = \dot{m}_{w,2}h_{w,2} - \dot{m}_{w,1}h_{w,1} \quad (4)$$

The total heat transfer rate between the air and water stream is the sum of the rate of sensible heat transfer by convection, q_{conv}, and the rate of heat transfer associated with condensation

$$\dot{m}_{w,2}h_{w,2} - \dot{m}_{w,1}h_{w,1} = q_{conv}dA + g_m[m_1(T_{a,1}) - m_1(T_{w,1})](h_{w,1} + h_{fg}(T_{w,1}))dA \quad (5)$$

where q_{conv} is expressed in terms of the temperature difference and the convective heat transfer conductance g_h

$$q_{conv} = g_h C_{p,a}(T_{a,1} - T_{w,1}) \quad (6)$$

The heat transfer conductance, g_h [in kg/(m^{2}s)], is defined as $h/C_{p,a}$ where h is the conventional heat transfer coefficient and $C_{p,a}$ is the specific heat of the saturated air. Since the range of temperature changes is relatively small, we assume that $C_{p,a}$ is constant. The Lewis number, *Le*, for water vapor and air is near unity. On the basis of the analogy between heat and mass transfer, we estimate the ratio of mass to heat transfer conductances to be $g_m/g_h \sim Le^{2/3} = 1.08$ (*27*).

For each experimental case, we solve Eqs. 2 to 6 using the measured water inlet temperature, $T_{w,in}$, and air outlet temperature, $T_{a,out}$, as inputs. We adjust the value of g_m iteratively until we match the measured temperature profiles for both the air and water streams. Figure S3 shows representative experimental temperature profiles and the corresponding best fits from Eqs. 2 to 6.

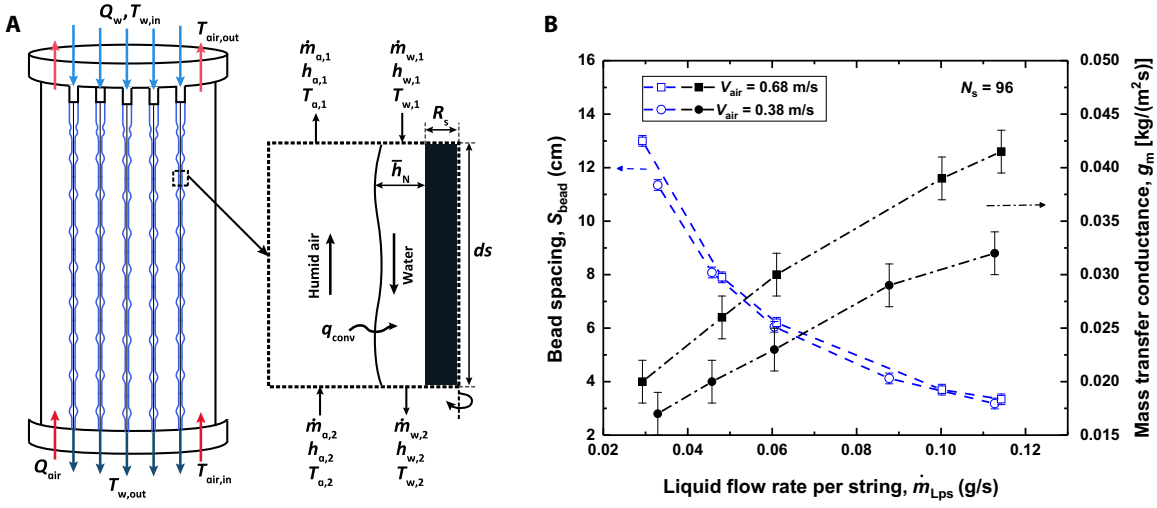

Fig. 3. Experimental mass transfer conductance. (**A**) Schematic of the control volume used to develop the governing mass and energy balance equations for the dehumidifier. (**B**) Mass transfer conductance and bead spacing as a function of the liquid flow rate per string under two different air stream velocities (V_{air} = 0.38 and 0.68 m/s).

Figure 3B shows the experimentally determined mass transfer conductance and water bead spacing as a function of the water flow rate under two different velocities of the counterflowing air. As the water mass flow rate increases, the bead spacing decreases and the total mass transfer conductance increases. To further analyze the effect of water beads on condensation rates in our experiments, we develop a simplified model. We decompose our liquid film conceptually into two components in a uniform air flow condition: (i) a thin continuous liquid substrate coating the thread and (ii) liquid beads of diameter D_{bead} sliding on the liquid substrate at speed V_{bead} in the range of 0.3 to 0.42 m/s. We model the liquid substrate as a stationary cylinder and each liquid bead as a sphere of the equivalent diameter (see Fig. 4A).

For mass transfer of water vapor from the humidified air stream to the sphere, we use the heat and mass transfer analogy to obtain the Sherwood number *Sh* (*27*, *28*)

$$\overline{\mathrm{Sh}}_{bead} = 2 + \left(0.4\,\mathrm{Re}_{bead}^{1/2} + 0.06\,\mathrm{Re}_{bead}^{2/3}\right) Sc^{0.4} \quad (7)$$

Here, the Reynolds number is $\mathrm{Re}_{bead} = \rho_m(V_{bead} + V_{air})D_{bead}/\mu$, where the superficial air velocity, V_{air}, is calculated by dividing the volumetric flow rate of air by the cross-sectional area provided by the acrylic cylinder with the diameter of 6.5 cm for the air stream. The dynamic viscosity of air is denoted by μ and the Schmidt number *Sc*. The mass transfer conductance for the bead, $\bar{g}_{m,bead}$, is next obtained from *Sh*

$$\bar{g}_{m,bead} = \rho_m \mathcal{D}_{12} \overline{\mathrm{Sh}}_{bead} \Big/ D_{bead} \quad (8)$$

Our liquid beads may not be represented as isolated spheres in a uniform gas flow. We use the existing correlation for $\bar{g}_{m,bead}$ only as a convenient and yet approximate expression to quantitatively interpret our experimental data. To assess the accuracy of the correlation for $\bar{g}_{m,bead}$, we numerically simulated air flows over an array of water beads flowing down a cotton thread. We find that, for relatively large inter-bead spacings (>6 times of the bead diameter), which is satisfied for all experimental conditions that we used, the impact of preceding liquid beads is relatively small. We estimate the error in $\bar{g}_{m,bead}$ calculated using

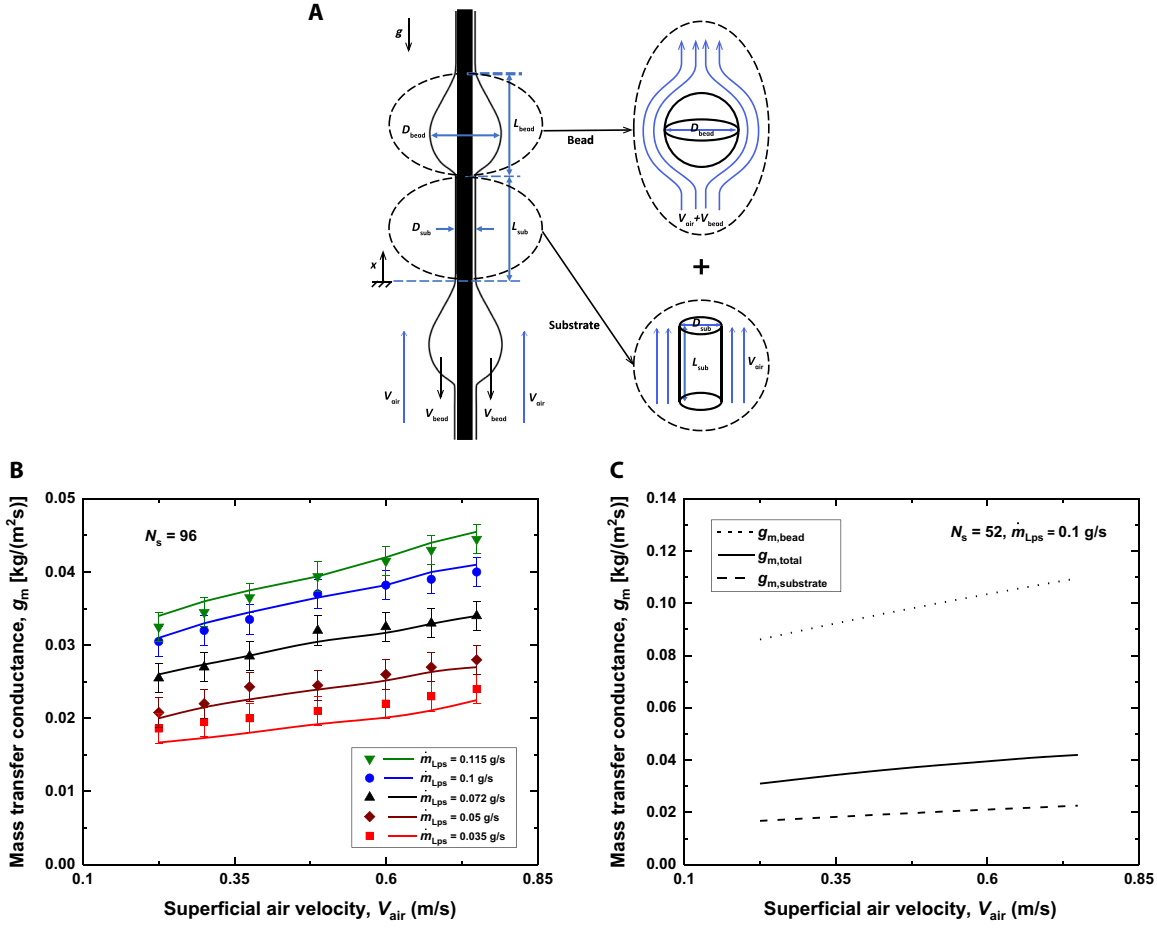

Fig. 4. Mass transfer conductance. (**A**) Schematic illustrating the decomposition of the water film into two components: (i) each water bead as a sphere in a uniform air stream of velocity $V_{air} + V_{bead}$ (to account for the bead velocity) and (ii) a stationary water cylinder with the same diameter as the liquid substrate coating the string in a uniform air stream of velocity V_{air}. (**B**) The experimental and predicted mass transfer conductances as a function of the superficial air velocity for the dehumidifier with 96 strings. Various sets of data are presented for different water flow rates per string, $\dot{m}_{Lps}$. The liquid flows are all in the RP regime. The symbols represent the experimental results, and the lines represent the model predictions. (**C**) The estimated mass transfer rate (in kg of water/s) to the total interfacial area of (i) liquid beads or (ii) the liquid substrate.

the existing correlation for an isolated sphere in a uniform gas flow to be less than 10%.

For the liquid substrate, we determine the mass transfer conductance $\bar{g}_{m,sub}$ by spatially averaging the local value from the boundary layer theory (section S2). The water-air interfacial area of the beads, A_{bead}, and that of the substrate, A_{sub}, are used as the weighting factors to calculate the overall g_m as follows

$$g_m = \frac{\bar{g}_{m,bead} \cdot A_{bead} + \bar{g}_{m,sub} \cdot A_{sub}}{A_{bead} + A_{sub}} \quad (9)$$

Figure 4B shows the experimentally determined and predicted mass transfer conductances of the design with 96 strings as a function of the superficial air velocity for various values of the water flow rates. We can observe that the predicted and measured mass transfer conductances agree to within 7%. The reasonably good agreement between the predicted and experimentally obtained g_m values indirectly supports the overall validity of our physical model for the heat and mass transfer processes involved. However, we do note that the water-air interfacial areas are needed as input parameters, which are obtained either from experiments or from a separate fluid mechanics model. Our results suggest that the mass transfer conductance for the beads is up to five times of that of the substrate (see Fig. 4C). This finding is in accord with the previous studies of condensation on localized surface bumps, which were inspired by desert beetles, where the importance of surface features on condensation rates was suggested (*29*). This enhanced mass transfer around water beads explains high mass transfer rates and hence correspondingly high condensation rates obtained in our experiments.

From Fig. 4B, one might expect that one could continue to increase the mass transfer and hence condensation rate by further increasing $\dot{m}_{Lps}$. When the water flow rate is increased above 0.135 g/s, however, the flow transitions into the convective instability regime and we observe a different trend (fig. S4A). As mentioned before, the transition to the convective instability regime results in bigger and faster moving beads. The increased bead diameter leads to a reduction in the mass transfer conductance around each bead, while the increased bead spacing leads to a reduction in the spatial density of liquid beads. These effects counteract enhancement resulting from the increased bead traveling speed (Eqs. 7 and 8). As a result, the overall mass transfer conductance remains nearly unchanged after the further increase in the liquid flow rates.

Gas stream pressure drop

A key consideration in a dehumidification process, aside from the overall mass transfer and hence condensation rate, is axial pressure drop in the gas stream. In Fig. 5A, we compare the experimentally measured pressure drop in the air stream per unit length and the corresponding model prediction as a function of the superficial air velocity. The two results agree to within 6%. The prediction (section S3) is based, in part, on an established empirical correlation for longitudinal flows over an array of parallel solid cylinders (*30*–*32*). The maximum Reynolds number for air flows in our experiments is approximately 2400, comparable to the critical Reynolds number for transition to turbulence (2300). Reynolds number can be calculated from $\mathrm{Re} = \rho_m (V_{air} + V_{bead}) D_h/\mu$, where D_h is the hydraulic diameter of the air duct. In the laminar flow regime, the pressure drop exhibits an approximately linear dependence on the superficial air velocity.

Liquid beads in the present work have relatively low geometric profiles, resulting in smaller form drag than spherical droplets in the presence of a counterflowing gas flow. This was confirmed in an independent experimental study of heat transfer in a multistring heat exchanger using nonevaporating liquids. In that study, the Reynolds analogy was shown to hold reasonably well, indicating that the frictional component to the pressure drop dominates over the component associated with form drag (*18*).

As the counterflowing air stream velocity, aerodynamic drag does deform liquid beads and change bead spacing (fig. S5). However, notable deformation does not occur until the air velocity is increased well beyond the range expected of typical dehumidification processes.

Overall performance

To quantify the overall performance of our device, we define the overall capacity coefficient, $g_m A_{int}/V_{deh}$, as our device performance parameter (*33*). Here, A_{int} and V_{deh} are the total liquid-gas interfacial area and the total volume of the device, respectively. This parameter essentially conveys the total mass transfer rate per unit volume of a dehumidifier.

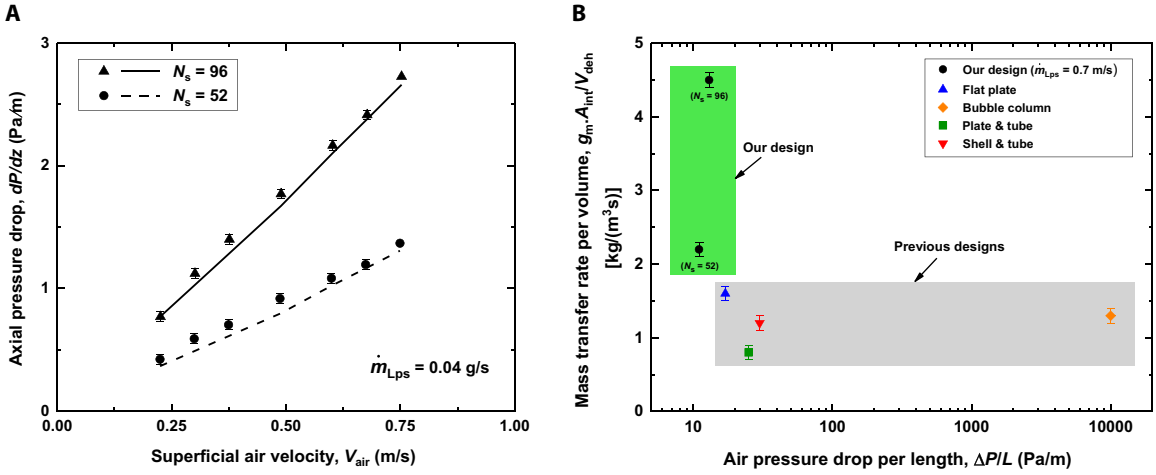

Fig. 5. Overall performance and pressure drop. (**A**) Pressure drop as a function of the superficial air velocity for the dehumidifiers with 52 and 96 strings. Symbols represent the experimental data, and the lines represent the model results. (**B**) Comparison of the mass transfer rate per volume as a function of the air pressure drop per length of dehumidifier. We compare our geometric configuration with previously reported dehumidifier designs, such as flat plate (*34*), bubble column (*35*), plate tube (*36*), and shell and tube (*37*). deh, dehumidifier.

Figure 5B shows the overall capacity coefficient of our design compared with that of other dehumidifiers as a function of the total gas stream pressure drop. We note that our unique geometric configuration offers at least three times higher overall capacity coefficients compared with existing designs at smaller air stream pressure drops. One might argue that the air and water mass flow rates can affect the overall capacity performance. However, this substantial improvement in the overall capacity coefficient is due to the ability of our compact design to provide intrinsic surface bumps, high interface-to-volume ratios for mass transfer, and the long resistance time for water vapor capturing due to the shear stress at the string surface. To ensure the fairness of our comparison in Fig. 5B, the results representing the other existing designs are obtained from conditions comparable with our experimental condition (see table S1).

Although previous studies did not report the weight of their humidifiers, we expect that the present humidifier, constructed of a plastic housing and cotton threads, also provides a remarkable weight reduction from established metal-based dehumidifiers. A further discussion and detailed calculation of the performance of our design and other established dehumidifier designs, specified in terms of the overall capacity coefficient ($g_m A_{int}/V_{deh}$), the total heat flux ($\dot{q}$), and the energy-based effectiveness (ε) are provided in section S4.

DISCUSSION

In summary, we have demonstrated the ability of our water vapor–capturing design in being able to substantially increase the condensation rate per device volume (200% increase), by taking advantage of high mass transfer rates of surface bumps while having the capability to remarkably decrease the air stream pressure drop by providing straight paths for gas flow, compared with the current dehumidifiers.

In the present work, liquid beads are generated through intrinsic instability of thin liquid films flowing down vertical cotton threads. No high-pressure spray nozzles or electric and other excitations are therefore necessary. Generating droplets of a narrow and controlled size distribution in spray columns is very challenging. Larger droplets are remarkably undesirable because they have higher fall velocities (shorter residence times) and larger internal thermal resistance, negatively affecting overall heat/mass transfer effectiveness. Very small droplets are also undesirable because they may be entrained by gas flows and then may mix with condensates in the dehumidifier, which is problematic because of the degrading quality of "clean" water output.

Furthermore, the models developed in this study are the starting point for further optimizing the design parameters of our device and achieving high-efficiency dehumidifier as a crucial component for decentralized thermal desalination and water vapor–capturing systems.

MATERIALS AND METHODS

Experimental design

Figure S7 shows the schematic of the experimental setup used in our study. The setup includes three flow loops: (i) the freshwater loop in the dehumidifier (dashed line), (ii) the air loop through the heater and the bubble column to achieve a specific humidity and temperature and finally along the dehumidifier (dotted line), and (iii) the closed water loop between the water heater and the bubble column for controlling the water temperature in the bubble column (dash-dotted line).

The dehumidifier consists of a 0.6-m-long vertical cylinder with a diameter of 2.5 inch and includes a square array of 52 (or 96) cotton threads with a 7-mm (or 5-mm) pitch. The cotton threads with a diameter of 0.76 mm were fixed to the bottom acrylic sheet to ensure their verticality. The liquid reservoir was located at the top. To introduce water onto the cotton threads, stainless steel nozzles with an inner diameter of 1.2 mm were used in our dehumidifier design and throughout this study, except in Fig. 1 for which we used a nozzle with an inner diameter of 0.8 mm. The inlet plenum at the bottom was designed to create a uniform flow of humidified air stream. Distilled water at 20°C (monitored using two thermocouples inside the reservoir) was pumped to the top reservoir from a main reservoir (FWR-1). A pump and a flow meter were used to control the flow rate. Water flows down the cotton threads after exiting the nozzles and absorbs the water vapor from the countercurrent humidified air stream. It was then collected at the bottom reservoir (FWR-2). A weight scale was placed under the freshwater reservoir (FWR-2), with a resolution of 0.1 g to measure the flow rate of freshwater at the outlet of dehumidifier.

We used a bubble column as a humidifier to supply air saturated with water to the dehumidifier. Filtered compressed air at 20°C flows into the bottom chamber of a bubble column, which has the cross section of 150 mm by 150 mm and height of 250 mm. The sieve plate has a square array of 25 by 25 holes with a diameter of 1 mm. Heated water circulates through the bubble column using a heating/pumping unit to ensure the uniform temperature distribution of water inside the bubble column. By adjusting the height of the heated water in the bubble column, a desired output air condition was obtained. The humidified air flows through two plastic tubes with an inner diameter of 25 mm to reach the air inlet of the dehumidifier.

Four sets of four microthermocouples with a tip diameter of 250 μm were mounted at four axial locations (0.0, 0.1, 0.4, and 0.7 m from the liquid nozzle) and four positions in each axial location (two for air temperature and two for water temperature), as shown in fig. S7 (locations 1 to 4). A differential pressure transducer (P) was used to measure air stream pressure drop along the 0.5-m-long mid-section of the dehumidifier. Two humidity sensors were also mounted at the air inlet and outlet of the dehumidifier to measure the relative humidity of air.

Data acquisition: Temperature, humidity, and pressure measurements

For each run, we first adjusted the water ($\dot{m}_{Lps}$ = 0.03 to 0.14 g/s) and air (V_{air} = 0.2 to 0.75 m/s) flow rates in flow loops (i) and (ii). Then, we started flow loop (iii) and waited for all the thermocouples, humidity sensors, and pressure transducer readings to stabilize to within 1% of their values before taking measurements. Each set of experiments was repeated multiple times to ensure repeatability. The uncertainties of the measured values were estimated as follows: ±0.1°C for the temperature readings, 0.03 Pa for the pressure readings, 0.1 g/s for the water flow rates at the outlet of dehumidifier, 1% for the relative humidity readings, and 0.05 m/s for the air velocities in the dehumidifier.

SUPPLEMENTARY MATERIALS

Supplementary material for this article is available at http://advances.sciencemag.org/cgi/content/full/5/4/eaav7662/DC1

Section S1. Full Navier-Stokes numerical simulation
Section S2. Mass transfer conductance of water substrate
Section S3. Air side pressure drop model
Section S4. Effectiveness, heat flux, and overall performance comparison
Fig. S1. Spatiotemporal diagram.
Fig. S2. Numerical simulation domain.
Fig. S3. Axial temperature profiles of the water and air streams.

Fig. S4. The effect of the flow regimes on mass transfer.
Fig. S5. Dynamics of water films flowing in countercurrent flows of air.
Fig. S6. Effectiveness and heat flux of dehumidifier.
Fig. S7. Experimental setup.
Table S1. Dehumidifier comparison.
References (*38*–*40*)

REFERENCES AND NOTES

1. M. M. Mekonnen, A. Y. Hoekstra, Four billion people facing severe water scarcity. *Sci. Adv.* **2**, e1500323 (2016).
2. A. R. Parker, C. R. Lawrence, Water capture by a desert beetle. *Nature* **414**, 33–34 (2001).
3. F. Fathieh, M. J. Kalmutzki, E. A. Kapustin, P. J. Waller, J. Yang, O. M. Yaghi, Practical water production from desert air. *Sci. Adv.* **4**, aat3198 (2018).
4. M. Damak, K. K. Varanasi, Electrostatically driven fog collection using space charge injection. *Sci. Adv.* **4**, aao5323 (2018).
5. A. Giwa, N. Akther, A. A. Housani, S. Haris, S. W. Hasan, Recent advances in humidification dehumidification (HDH) desalination processes: Improved designs and productivity. *Renew. Sustain. Energy Rev.* **57**, 929–944 (2016).
6. G. Prakash Narayan, J. H. Lienhard, S. M. Zubair, Entropy generation minimization of combined heat and mass transfer devices. *Int. J. Therm. Sci.* **49**, 2057–2066 (2010).
7. G. Prakash Narayan, M. G. St. John, S. M. Zubair, J. H. Lienhard V, Thermal design of the humidification dehumidification desalination system: An experimental investigation. *Int. J. Heat Mass Transf.* **58**, 740–748 (2013).
8. K. M. Chehayeb, G. P. Narayan, S. M. Zubair, J. H. Lienhard V, Thermodynamic balancing of a fixed-size two-stage humidification dehumidification desalination system. *Desalination* **369**, 125–139 (2015).
9. K. M. Chehayeb, G. Prakash Narayan, S. M. Zubair, J. H. Lienhard V, Use of multiple extractions and injections to thermodynamically balance the humidification dehumidification desalination system. *Int. J. Heat Mass Transf.* **68**, 422–434 (2014).
10. W. M. Rohsenow, J. P. Hartnett, "*Handbook of heat transfer*" (McGraw-Hill Book Company, 1973); www.osti.gov/biblio/4324656-handbook-heat-transfer.
11. J. Huang, J. Zhang, L. Wang, Review of vapor condensation heat and mass transfer in the presence of non-condensable gas. *Appl. Therm. Eng.* **89**, 469–484 (2015).
12. T. D. Karapantsios, A. J. Karabelas, Direct-contact condensation in the presence of noncondensables over free-falling films with intermittent liquid feed. *Int. J. Heat Mass Transf.* **38**, 795–805 (1995).
13. M. K. Bologa, I. K. Savin, A. B. Didkovsky, Electric-field-induced enhancement of vapour condensation heat transfer in the presence of a non-condensable gas. *Int. J. Heat Mass Transf.* **30**, 1577–1585 (1987).
14. G. P. Narayan, M. H. Sharqawy, S. Lam, S. K. Das, J. H. Lienhard, Bubble columns for condensation at high concentrations of noncondensable gas: Heat-transfer model and experiments. *AIChE J.* **59**, 1780–1790 (2013).
15. K. Hattori, M. Ishikawa, Y. H. Mori, Strings of liquid beads for gas–liquid contact operations. *AIChE J.* **40**, 1983–1992 (1994).
16. K. Uchiyama, H. Migita, R. Ohmura, Y. H. Mori, Gas absorption into "string-of-beads" liquid flow with chemical reaction: Application to carbon dioxide separation. *Int. J. Heat Mass Transf.* **46**, 457–468 (2003).
17. H. Chinju, K. Uchiyama, Y. H. Mori, "String-of-beads" flow of liquids on vertical wires for gas absorption. *AIChE J.* **46**, 937–945 (2000).
18. Z. Zeng, A. Sadeghpour, Y. S. Ju, Thermohydraulic characteristics of a multi-string direct-contact heat exchanger. *Int. J. Heat Mass Transf.* **126**, 536–544 (2018).
19. Z. Zeng, A. Sadeghpour, Y. S. Ju, A highly effective multi-string humidifier with a low gas stream pressure drop for desalination. *Desalination* **449**, 92–100 (2019).
20. C. Duprat, C. Ruyer-Quil, S. Kalliadasis, F. Giorgiutti-Dauphiné, Absolute and convective instabilities of a viscous film flowing down a vertical fiber. *Phys. Rev. Lett.* **98**, 244502 (2007).
21. C. Ruyer-Quil, P. Treveleyan, F. Giorgiutti-Dauphiné, C. Duprat, S. Kalliadasis, Modelling film flows down a fibre. *J. Fluid Mech.* **603**, 431–462 (2008).
22. C. Duprat, C. Ruyer-Quil, F. Giorgiutti-Dauphiné, Experimental study of the instability of a film flowing down a vertical fiber. *Eur. Phys. J. Spec. Top.* **166**, 63–66 (2009).
23. C. Duprat, C. Ruyer-Quil, F. Giorgiutti-Dauphiné, Spatial evolution of a film flowing down a fiber. *Phys. Fluids* **21**, 042109 (2009).
24. C. Duprat, D. Tseluiko, S. Saprykin, S. Kalliadasis, F. Giorgiutti-Dauphiné, Wave interactions on a viscous film coating a vertical fibre: Formation of bound states. *Chem. Eng. Process.* **50**, 519–524 (2011).
25. M. J. Miksis, S. H. Davis, Slip over rough and coated surfaces. *J. Fluid Mech.* **273**, 125–139 (1994).
26. F. J. Solorio, M. Sen, Linear stability of a cylindrical falling film. *J. Fluid Mech.* **183**, 365–377 (1987).
27. S. Whitaker, Forced convection heat transfer correlations for flow in pipes, past flat plates, single cylinders, single spheres, and for flow in packed beds and tube bundles. *AIChE J.* **18**, 361–371 (1972).
28. A. Mills, *Heat and Mass Transfer* (CRC Press, 1995).
29. K.-C. Park, P. Kim, A. Grinthal, N. He, D. Fox, J. C. Weaver, J. Aizenberg, Condensation on slippery asymmetric bumps. *Nature* **531**, 78–82 (2016).
30. E. M. Sparrow, A. L. Loeffler Jr., Longitudinal laminar flow between cylinders arranged in regular array. *AIChE J.* **5**, 325–330 (1959).
31. K. Rehme, Pressure drop performance of rod bundles in hexagonal arrangements. *Int. J. Heat Mass Transf.* **15**, 2499–2517 (1972).
32. K. Rehme, G. Trippe, Pressure drop and velocity distribution in rod bundles with spacer grids. *Nucl. Eng. Des.* **62**, 349–359 (1980).
33. H. Migita, K. Soga, Y. H. Mori, Gas absorption in a wetted-wire column. *AIChE J.* **51**, 2190–2198 (2005).
34. M. Sievers, J. H. Lienhard V, Design of flat-plate dehumidifiers for humidification–dehumidification desalination systems. *Heat Transf. Eng.* **34**, 543–561 (2013).
35. E. W. Tow, J. H. Lienhard V, Experiments and modeling of bubble column dehumidifier performance. *Int. J. Therm. Sci.* **80**, 65–75 (2014).
36. M. M. Farid, S. Parekh, J. R. Selman, S. Al-Hallaj, Solar desalination with a humidification-dehumidification cycle: Mathematical modeling of the unit. *Desalination* **151**, 153–164 (2003).
37. Z. Chang, H. Zheng, Y. Yang, Y. Su, Z. Duan, Experimental investigation of a novel multi-effect solar desalination system based on humidification–dehumidification process. *Renew. Energy* **69**, 253–259 (2014).
38. D. M. Warsinger, K. H. Mistry, K. G. Nayar, H. W. Chung, J. H. Lienhard V, Entropy generation of desalination powered by variable temperature waste heat. *Entropy* **17**, 7530–7566 (2015).
39. G. P. Narayan, K. H. Mistry, M. H. Sharqawy, S. M. Zubair, J. H. Lienhard, Energy effectiveness of simultaneous heat and mass exchange devices. *Front. Heat Mass Transf.* **1**, 1–13 (2010).
40. R. W. Hyland, A. Wexler, Formulations for the thermodynamic properties of dry air from 173.15 K to 473.15 K, and of saturated moist air from 173.15 K to 372.15 K, at pressures to 5 MPa. *ASHRAE Trans.* **89**, 520–535 (1980).

Acknowledgments

Funding: Z.Z., A.S., and Y.S.J. were supported by the U.S. NSF under grant CBET-1358034. A.S., H.J., and A.B. were supported by the Simons Foundation Math+X Investigator Award number 510776. **Author contributions:** A.S., Z.Z., and Y.S.J. designed and performed the experiments. All authors analyzed and interpreted the experimental data. Y.S.J. conceived and supervised the project. A.S., Z.Z., H.J., A.L.B., and Y.S.J. wrote the manuscript. **Competing interests:** The authors are preparing patent applications based, in part, on the results presented in the paper, but no formal patent applications have been filed at this time. The authors declare that they have no other competing interests. **Data and materials availability:** All data needed to evaluate the conclusions in the paper are present in the paper and/or the Supplementary Materials. Additional data related to this paper may be requested from the authors.

Submitted 17 November 2018
Accepted 20 February 2019
Published 12 April 2019
10.1126/sciadv.aav7662

Citation: A. Sadeghpour, Z. Zeng, H. Ji, N. Dehdari Ebrahimi, A. L. Bertozzi, Y. S. Ju, Water vapor capturing using an array of traveling liquid beads for desalination and water treatment. *Sci. Adv.* **5**, eaav7662 (2019).